Resistivity Index Mapping in Kidney Based on Ultrasensitive Pulsed-Wave Doppler and Automatic Spectrogram Envelope Detection

Lenin Chinchilla, Thomas Frappart, Christophe Fraschini, Jean-Michel Correas, Jean-Luc Gennisson

Resistivity Index Mapping in Kidney Based on Ultrasensitive Pulsed-Wave Doppler and Automatic Spectrogram Envelope Detection

Lenin Chinchilla, Thomas Frappart, Christophe Fraschini, Jean-Michel Correas, and Jean-Luc Gennisson, *Member, IEEE*

***Abstract*—In recent years, ultrasensitive pulsed-wave Doppler (uPWD) ultrasound (US) has emerged as an alternative imaging approach for microcirculation imaging and as a complementary tool to other imaging modalities, such as positron emission tomography (PET). uPWD is based on the acquisition of a large set of highly spatiotemporally coherent frames, which allows high-quality images of a wide field of view to be obtained. In addition, these acquired frames allow calculation of the resistivity index (RI) of the pulsatile flow detected over the entire field of view, which is of great interest to clinicians, for example, in monitoring the transplanted kidney course. This work aims to develop and evaluate a method to automatically obtain an RI map of the kidney based on the uPWD approach. The effect of time gain compensation (TGC) on the visualization of vascularization and aliasing on the blood flow frequency response was also assessed. A pilot study conducted in patients referred for renal transplant Doppler examination showed that the proposed method provided relative errors of about 15% for RI measurements with respect to conventional pulsed-wave (PW) Doppler.**

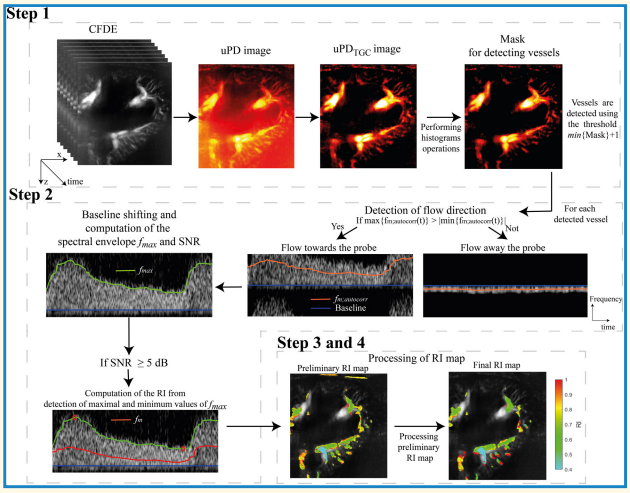

***Index Terms*—Microcirculation imaging, renal transplantation, resistivity index (RI), ultrasensitive pulse Doppler.**

I. Introduction

IN RECENT years, ultrasensitive pulsed-wave Doppler (uPWD) ultrasound (US) has emerged as an alternative imaging approach for microcirculation imaging [1], [2], [3], [4] and as a complementary tool to other imaging modalities, such as positron emission tomography (PET) [5], [6]. This method is based on ultrafast plane wave imaging with multiple-angle compounding, which enables the acquisition of a large set of highly spatiotemporal coherent frames, allowing high-quality imaging of a wide field of view. uPWD provides detection of blood flow, from which the spectrogram can be computed using the clutter-filtered Doppler ensemble (CFDE) [3]. Using this spectrogram, quantitative measurements, such as the resistivity index (RI), could be obtained in an automatic way in a wide region of interest. RI color maps can be displayed, in contrast with the current method where single RI measurements are obtained from a single vessel.

The renal RI has been used for the assessment of kidney state [7], [8], [9]; however, recent evidence has shown that renal RI is also related to inherent hemodynamic characteristics of patients [10], [11]. This suggests that only the use of RI in certain regions of the kidney, as currently performed, as an indicator of kidney malfunction might be biased. Therefore, new approaches to RI measurement and combination with other biomarkers could improve the interpretation of renal RI for diagnosis. Thus, the aim of this work is to propose and evaluate a method to automatically obtain an RI map in the

Manuscript received 7 December 2022; accepted 23 January 2023. This work was supported by the Bettencourt Schueller Foundation through the project name: PERFUSION in the Biomedical Engineering Chair from the École Polytechnique. *(Corresponding author: Jean-Luc Gennisson.)*

This work involved human subjects or animals in its research. Approval of all ethical and experimental procedures and protocols was granted by the Institutional Review Board of the Comite d'ethique de la recherche en imagerie medicale (CERIM), under Application No. IRB CRM-2203-244.

Lenin Chinchilla and Jean-Luc Gennisson are with the Laboratoire d'imagerie biomédicale multimodale, BioMaps, Commissariat à l'Energie Atomique et aux Energies Alternatives (CEA), French National Research Center (CNRS), Inserm, Université Paris-Saclay, 91400 Orsay, France (e-mail: lenin.chinchilla-atencia@universite-paris-saclay.fr; jean-luc.gennisson@universite-paris-saclay.fr).

Thomas Frappart and Christophe Fraschini are with Hologic, 13290 Aix-en-Provence, France (e-mail: Thomas.Frappart@hologic.com; Christophe.Fraschini@hologic.com).

Jean-Michel Correas is with the Biomedical Imaging Laboratory, UMR 7371–U114, University of Paris, 75006 Paris, France (e-mail: jean-michel.correas@aphp.fr).

Digital Object Identifier 10.1109/TUFFC.2023.3240283

Highlights

- **We developed a methodology to automatically obtain a 2-D color resistivity index map of the renal vasculature, based on the ultrafast ultrasound Doppler approach and using a clinic ultrasound scanner.**
- **Results of the proposed method in patients referred for renal transplant Doppler examination provided relative errors of less than 15% for RI measurements compared with conventional pulsed-wave Doppler.**
- **The proposed method provides the information currently required by clinicians, and visualization of pulsatile regions with corresponding resistivity index, which could be useful for diagnostic purposes.**

kidney based on uPWD, which could provide new insights to better interpret renal RI.

Obtaining an RI map based on the uPWD approach has already been studied for the neonatal brain [3], [12] and liver [13]. As far as we know, this is the first time that an RI map for the kidney is intended to be obtained automatically. However, an RI map in deep organs, such as kidneys, remains challenging as the detection of vessels, the computation of the spectrogram envelope (or maximal flow velocity), can be strongly affected by the movement and attenuation of the Doppler spectrum. For instance, Song et al. [14], [15] showed that time gain compensation (TGC) plays an important role in uPWD as it increases the inherent channel noise, leading to the degradation of flow signal visualization in the deep field where blood signals and noise present similar amplitudes. Therefore, uPWD is affected by spatially varying background noise. Some of the methods to automatically detect spectrogram envelope are spectral-based approaches, which relies on noise threshold estimation [16] and variants [17], [18]. These techniques require a proper detection of the baseline, which must be performed manually prior to envelope detection. Moreover, in uPWD, the baseline changes from one point to another as it is affected by aliasing effects. Therefore, the detection and subsequent mitigation of these undesirable effects are necessary in order to obtain an RI map.

In the method proposed in this work, the ultrasensitive power Doppler (uPD) image is improved by using a strategy to compensate for TGC effects based on the equalization approach [15], [19], [20], [21], [22], [23], [24], [25], which does not assume homogeneity of the background noise through the channels. Then, a method adapted to signals from the kidney is presented to automatically detect the spectrogram envelope, where issues related to aliasing effects are addressed. The improved power Doppler image is used jointly with the proposed detection envelope algorithm to obtain the RI map. The proposed method to compute the RI is evaluated using simulated power Doppler spectrograms, as well as in vivo acquisitions. In this work, some of the methods previously presented in [25] were used. However, this work presents notable differences with respect to the one presented in [25] in the obtaining and processing of the RI map, the algorithm for envelope detection, which is better adapted and faster, and the use of a larger group of patients.

This work is organized as follows. Section II describes conventional pulsed-wave (PW) Doppler acquisitions (hereinafter referred to as PW Doppler), procedures to perform simulations and obtain the uPD image and envelope detection, and comparison between RI measurements performed by using PW Doppler and the proposed method. Section III presents results of RI obtained from simulations that are used to evaluate the proposed method for measuring the RI, followed by results of the RI map and its comparison with PW Doppler measurements, followed by discussion and conclusion.

II. Materials and Methods

A. In Vivo Acquisitions

The Aixplorer V12 ultrafast US system (Supersonic Imagine, Aix-en-Provence, France) was used to perform specific acquisitions on renal transplants, in patients referred for renal Doppler examination. A total of five patients were recruited and gave written informed consent according to the ethical protocol # IRB CRM-2203-244, which was approved by the institutional review board of the Comité d'éthique de la recherche en imagerie médicale (CERIM), Paris, France. An ultrafast US sequence was developed consisting of two insonification angles ($-2°$ and $2°$), with a compounded pulse repetition frequency (PRF) of 2000 Hz, using a linear transducer (L10-2) with a center frequency of 5.8 MHz. The acquisitions included routine evaluation of the transplanted kidney using B-mode and conventional color Doppler US imaging, followed by PW Doppler interrogation of several interlobular arteries, including calculation of the local RI. Color Doppler US is used to detect the position of the vessel and PW Doppler performed by moving the Doppler gate upon a vessel of pulsatile flow. The radiologist determines the peak systolic and end-diastolic velocities to calculate the RI. In a subsequent step, the same US machine and probe were used at approximately the same location to collect data with the developed sequence in the acquisitions of 1-s duration. For all acquisitions, patients were asked to hold their breath.

Spectrograms and the corresponding RI from PW Doppler were recorded in at least three different regions of the kidney for each patient. These measurements were used to evaluate the obtained RI map.

B. Simulations

The simulated Doppler signals were generated based on the approach proposed by Mo and Cobbold [26] and using typical spectrograms of acquired data from transplanted patients. In brief, Mo and Cobbold [26] proposed a method to generate

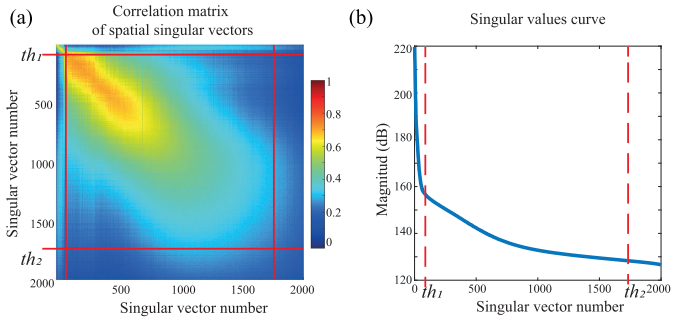

Fig. 1. Thresholds used for SVD filtering for patient 2, shown on (a) correlation pattern of spatial singular vectors (correlation matrix of spatial singular vectors) and (b) singular values' curve.

a synthetic time sequence from a smoothed measured power spectral density (PSD) that extends in the range $[0, f_{\max}]$, calculated from acquisitions of about 10 ms of duration. Thus, each realization of a synthetic time sequence Doppler signal is computed as the concatenation of segments of 10 ms, $x(t)$, computed as

$$x(t) = \sum_{m=1}^{M} a_m \cos(2\pi f_m t + \phi_m) \tag{1}$$

where

$$f_m = \left(m - \frac{1}{2}\right)\frac{f_{\max}}{M}, \quad m = 1, 2, \ldots, M \tag{2}$$

and

$$a_m = \sqrt{\frac{2}{M}\mathrm{PSD}(f_m)\, f_{\max} y_m} \tag{3}$$

in which $(f_{\max}/M)$ and the set of values y_m are independent chi-square random variables with two degrees-of-freedom, and ϕ_m values are random variables each uniformly distributed over $[0, 2\pi]$. Statistical analysis was performed by considering a set of ten signals, where each signal consisted of an average of one, nine, or 200 realizations.

C. Ultrasensitive PW Doppler Processing

1) Clutter Filtering: Each ultrasensitive Doppler acquisition provides an ensemble of N_t frames, IQ, from which the CFDE, $\mathrm{IQ}_{\mathrm{blood}}$, is obtained using a singular value decomposition (SVD) thresholding approach [3] as

$$\mathrm{IQ}_{\mathrm{blood}}(x, z, t) = \mathrm{IQ}(x, z, t) - \left(\sum_{k=1}^{k=\mathrm{th}_1} U_k \lambda_k V_k^* + \sum_{k=\mathrm{th}_2}^{k=N_t} U_k \lambda_k V_k^*\right) \tag{4}$$

where th_1 and th_2 represent the singular value thresholds, corresponding to clutter and noise signals, respectively. These thresholds were selected manually for each acquisition based on the correlation pattern of spatial singular vectors [27]. Fig. 1 shows, as an example, the thresholds used for SVD filtering for patient 2 on the correlation pattern of spatial singular vectors, and the singular values' curve.

2) Ultrasensitive Power Doppler Image: Using the CFDE, the uPD image is computed as

$$\mathrm{uPD}(x, z) = \frac{1}{N_t}\sum_{t=1}^{N_t} |\mathrm{IQ}_{\mathrm{blood}}(x, z, t)|^2. \tag{5}$$

The compensated uPD image for TGC effects, $\mathrm{uPD}_{\mathrm{TGC}}$, is computed as

$$\mathrm{uPD}_{\mathrm{TGC}}(x, z) = \frac{\mathrm{uPD}(x, z)}{N_{\mathrm{BKG}}(x, z)} \tag{6}$$

where $N_{\mathrm{BKG}}(x, z)$ is computed adaptively from the uPD image as follows.

First, the uPD image is downsampled in the axial direction by a factor of 7. Then, each column and then each row of the resulting image are smoothed using the *rlowess* algorithm of MATLAB (The MathWorks, Inc. MATLAB, Version 2020b). Finally, the smoothed subsampled image is interpolated in the axial direction back to the original size and then smoothed again using a 2-D Gaussian filter (with a standard deviation of 15). A more detailed description of the estimation of $N_{\mathrm{BKG}}(x, z)$ is presented in [25].

D. Computation of the Spectrogram Compensated for Aliasing Effects

The spectrogram, $\mathrm{SSTF}(x, z, f, t_0)$, is computed from the CFDE based on the short-time Fourier transformation as

$$\mathrm{SSTF}(x, z, f, t_0) = \left|\int_{t_0 - t_w/2}^{t_0 + t_w/2} \mathrm{IQ}(x, z, t') e^{-j2\pi f t'} W(t' - t_0) dt'\right|^2 \tag{7}$$

where $W(t)$ is a Hann window centered at 0 of duration t_w equal to 32 points (16 ms at a sampling frequency $f_s = 2000$ Hz). SSTF is computed from times $t_0 = t_w/2$ to $t_0 = \Delta t_{\mathrm{total}} - t_w/2$ with a lag of two samples, where $\Delta t_{\mathrm{total}}$ is the total duration of signal in t.

The baseline is automatically detected, and the spectrogram is shifted accordingly to compensate for aliasing effects.

The procedure to obtain this corrected spectrogram, $\mathrm{SSTF}_{\mathrm{corr}}$, was presented in [25], and a more detailed description is given in the Appendix.

E. Envelope Detection: Modified Threshold Method (MTM)

The detection of the spectrogram envelope, or equivalently the maximum frequencies, $f_{\max}(t_0)$, is performed following a spectrum-based approach [17], [28], where a signal region and a noise region are defined, and the maximum frequency between these regions, commonly referred to as the knee region, is searched for.

In the MTM, the following assumptions are made.

1) The absolute value of the largest frequency corresponds to $f_s - 100$.
2) No aliasing is present in the signal.

Fig. 2 depicts the procedure to estimate $f_{\max}(t_0)$. In summary, a first threshold, Thres_1, is estimated from the noise floor, noise_f, so that $f_{\max}(t_0)$ to a given time t_0 is set as the

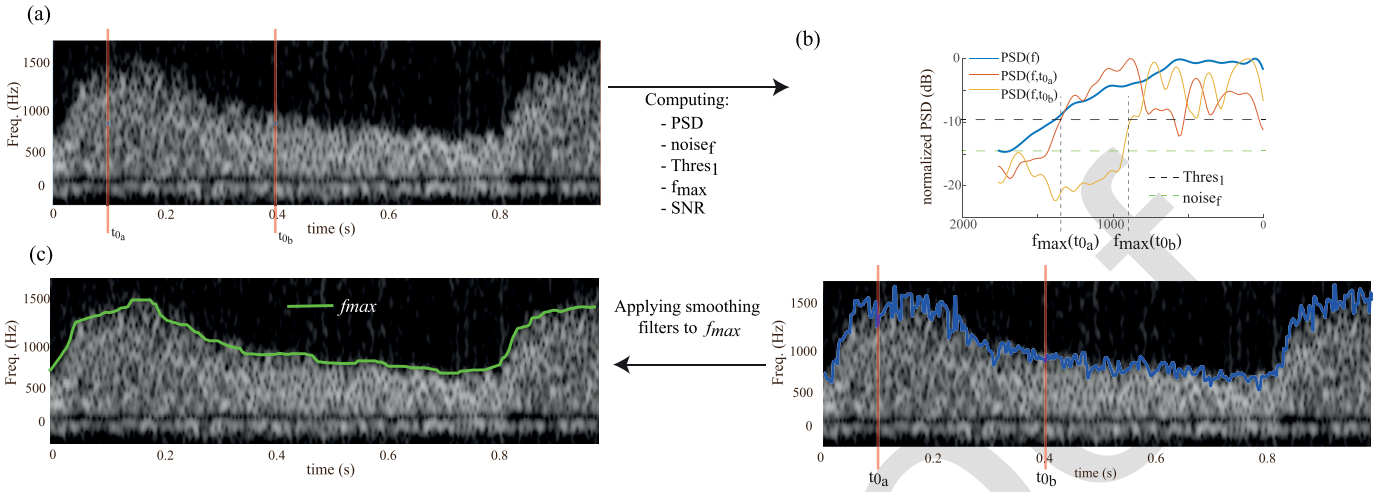

Fig. 2. Procedure to perform the envelope detection based on the MTM algorithm. (a) Corrected spectrogram (compensated for aliasing effects). (b) Computation of the PSD from the spectrogram, from which threshold, Thres_1, is calculated based on the noise floor, noise_f, to determine the maximal frequency in function of time. (c) Estimated envelope after applying the smoothing filtering.

highest frequency at which the corresponding normalized PSD is above this threshold. More specifically, Thres_1 is defined as follows. If $\text{noise}_f < -18$ dB, $\text{Thres}_1 = -10$ dB, or if $\text{noise}_f < -10$ dB, $\text{Thres}_1 = \text{noise}_f/2 - 1.5$ dB; otherwise, $\text{Thres} = \text{noise}_f/2$.

This first envelope is then smoothed by a 64-point median filter (32 ms at a sampling rate of $f_s = 2000$ Hz). Using this smoothed envelope, the noise bins are calculated as the values of the side of the spectrogram related to the flow direction whose frequencies are higher than the calculated envelope. Using these values, the average noise power, $\langle N \rangle$, is calculated as the average of the values below the 90th percentile, and the SNR is calculated as

$$\text{SNR} = \frac{\langle S \rangle - \langle N \rangle}{\langle N \rangle} \tag{8}$$

where $\langle S \rangle$ corresponds to the average signal power, computed as the average of the spectrogram values on the side corresponding to the flow direction.

Both baseline and envelope detection algorithms were evaluated in terms of the number of realizations used to compute the spectrogram, SNR, and aliasing. Since the ground truth of the peak systolic and end-diastolic velocities, and consequently that of the RI, is unknown, we use the method *modified signal noise slope intersection* (MSNSI), proposed by Kathaplia et al. [17], to calculate the envelope of the spectrogram under the best conditions in terms of SNR, aliasing, and realizations. The calculation of the RI from this envelope is what we use as a benchmark in this study.

F. Resistivity Index Map Computation and Processing

Fig. 3 depicts the procedure to automatically obtain the RI map from the CFDE, which is obtained as follows.

Step 1: After clutter filtering, uPD and uPD_{TGC} images are obtained. The uPD_{TGC} image is used to define a mask with a homogeneous background that is obtained by applying histogram operations on the uPD_{TGC}: first, a thresholding operation, and then, a contrast stretching operation. Using this mask, the vessels are detected so that their intensity is greater than the background intensity value by 1 dB.

Step 2: For each detected vessel, the flow direction is calculated using the absolute maximum value of the axial velocity calculated by the autocorrelation method, $f_{m;\text{autocorr}}$. If the flow direction is away from the probe, the RI calculation is not performed. If the flow direction is toward the probe, the CFDE is used to calculate the corresponding spectrogram compensated for aliasing effects, from which the spectrogram envelope, $f_{\max}(t_0)$, is calculated by using the MTM algorithm proposed in this work, as well as the SNR. Only if the SNR is equal to or greater than 5 dB, the RI is calculated as

$$\text{RI} = \frac{\max_t[f_{\max}(t)] - \min_t[f_{\max}(t)]}{\max_t[f_{\max}]} \tag{9}$$

where $\min_t[\cdot]$ and $\max_t[\cdot]$ correspond to the minimum and maximum values' operators, $\min_t[f_{\max}(t)]$ represents the estimated end-diastolic velocity, and $\max_t[f_{\max}(t)]$ represents the estimated peak systolic velocity.

This RI value is checked by using the mean frequency, $f_m(t_0)$, computed as

$$f_m(t_0) = \frac{\int f' \text{SSTF}_{\text{corr}}(x, z, f', t_0) df'}{\int \text{SSTF}_{\text{corr}}(x, z, f', t_0) df'} \tag{10}$$

and the following criteria.

a) RI value has to be smaller than 1.
b) $\min_t[f_{\max}(t)]$ has to be greater than $f_m(t_{\min})$, with $t_{\min}$ being the time of occurrence of $\min_t[f_{\max}(t)]$. This is to avoid RI measurements where the end-diastolic velocity is not properly estimated.
c) Signals with SNR values smaller than 10 dB must have a value of $\max_t[f_{\max}(t)]$ less than 3/4 the sampling frequency. This threshold is based on simulations, which have shown that, in these cases,

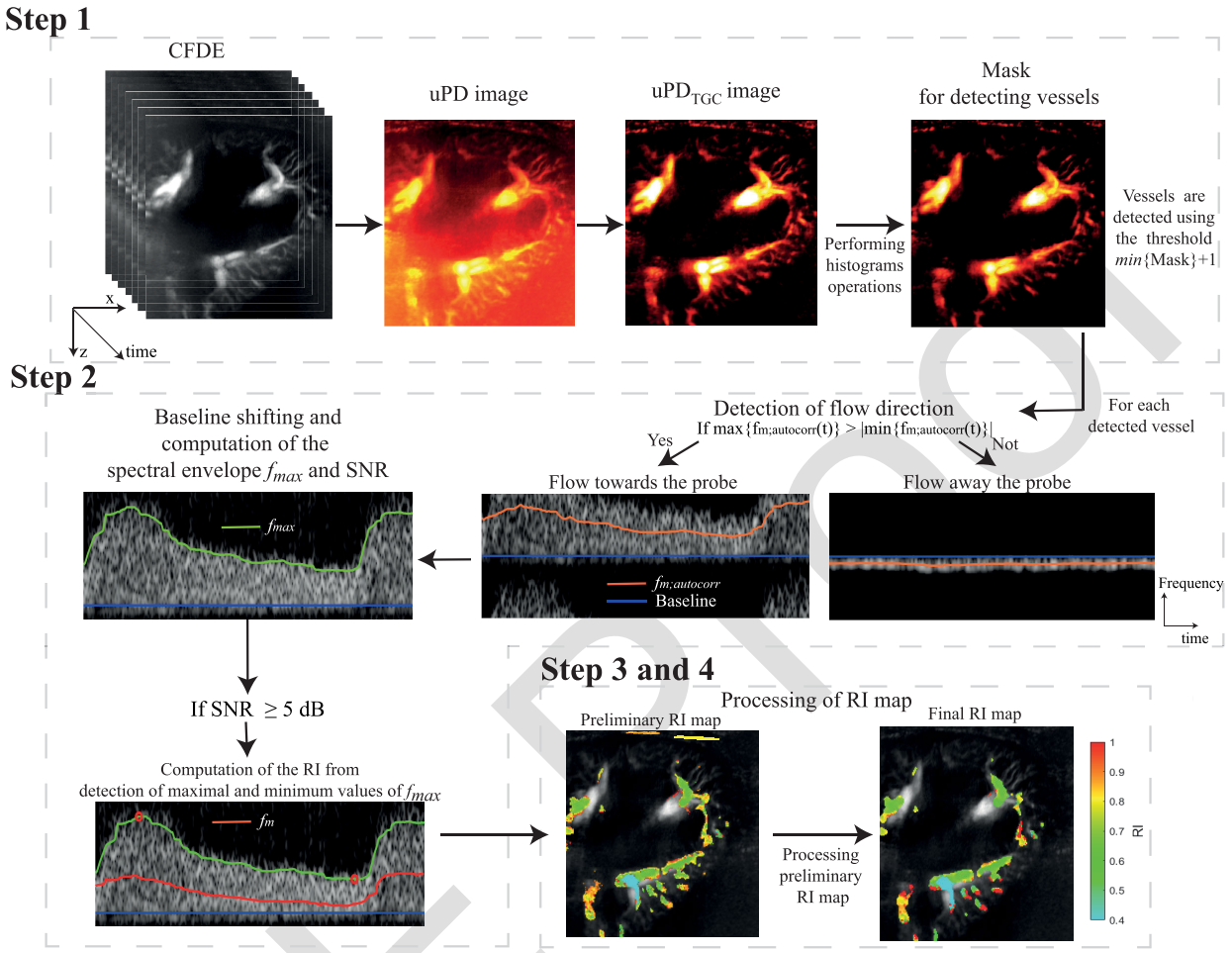

Fig. 3. Procedure to automatically obtain the RI map.

the RI measurements are inaccurate, as described in the results in Section III-A.

d) Signals with SNR values equal to or greater than 10 dB must have a value of $\max_t[f_{\max}(t)]$ less than the sampling frequency, f_s, minus 100 Hz. $f_s - 100$ represents the maximum detectable frequency.

If one of these conditions is not met, the RI is set to 1, which represents pulsatile flow regions where the RI calculation is unreliable. At the end of this step, a preliminary RI map is obtained.

Step 3: In this step, RI values less than 0.4 are adjusted to a minimum RI value of 0.4, which is considered a nonpulsatile flow, and would probably correspond to a vein.

Step 4: In this step, it is checked whether the RI values between 0.7 and 1 have a maximum mean frequency (this mean frequency is calculated by the autocorrelation method and differs from $f_m(t_0)$ defined above) higher than a certain threshold. This threshold is defined as the median of the maximum frequencies for the flow directions to the probe (regions with RI values equal to 1 and 0.4 are excluded for the calculation of these thresholds). Regions that do not meet this criterion are removed from the RI map. This helps to remove regions of false vessels, e.g., subcutaneous tissue. Finally, the RI map is smoothed using a 2-D median filter, where each output pixel contains the median value in the 3×3 neighborhood around the corresponding pixel.

RI measurements obtained with the proposed approach were compared to those obtained with PW Doppler: first, by comparing local measurements obtained approximately in the same region; second, by calculating the Pearson correlation coefficient between the median of the values given by the RI map and the measurements obtained by the PW Doppler approach.

All algorithms used to obtain the RI map were developed in MATLAB and were implemented using a computer system consisting of an Intel[1] Core i9 processor 2.3 GHz and 32 GB of RAM.

III. Results

A. Evaluation of Baseline and Envelope Detection Algorithms

Fig. 4 shows, as an example for a certain signal, results of compensation for aliasing effects and computation of the spectrogram envelope for the cases of different sampling

[1]Registered trademark.

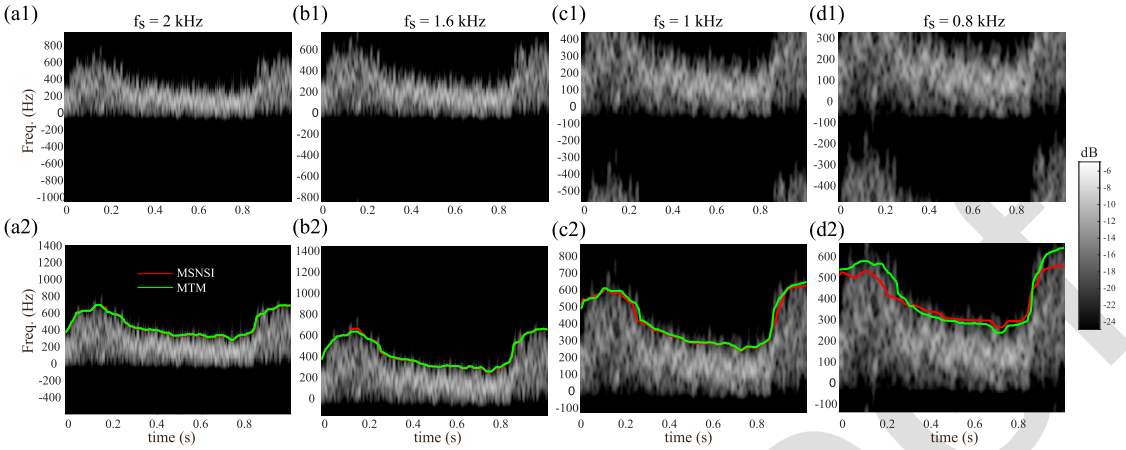

Fig. 4. Example of results of the aliasing compensation and envelope detection algorithms for the signal 1 with an SNR = 15 dB. (a1)–(d1) Spectrogram before aliasing compensation and (a2)–(d2) after aliasing compensation. Envelope detection is only performed after aliasing compensation.

TABLE I
RI COMPUTATIONS WHERE MEAN VALUES AND STANDARD DEVIATIONS OVER TEN ESTIMATES ARE SHOWN FOR THE DIFFERENT ANALYZED SIGNALS WITH SNR = 15 dB

	MSNSI			MTM		
	N_{rz} = 1	N_{rz} = 9	N_{rz} = 200	N_{rz} = 1	N_{rz} = 9	N_{rz} = 200
$Signal_1$	0.58 ± 0.03	0.60 ± 0.01	0.60 ± 0.01	0.59 ± 0.02	0.59 ± 0.01	0.59 ± 0.01
$Signal_2$	0.53 ± 0.03	0.55 ± 0.01	0.54 ± 0.01	0.55 ± 0.03	0.54 ± 0.01	0.54 ± 0.01
$Signal_3$	0.52 ± 0.04	0.50 ± 0.01	0.49 ± 0.01	0.41 ± 0.21	0.49 ± 0.01	0.49 ± 0.01

frequencies and SNR of 15 dB. Overall, it can be seen that the compensation for aliasing effects works quite well for the conditions tested, and the differences in the envelope of the spectrogram computed using MSNSI and MTM increase as the aliasing effects become more important. These differences will be discussed in more detail in the discussion (see Section IV).

The variability of the simulated RI was studied in terms of the number of realizations averaged to compute the spectrogram, N_{rz}, for the cases of one, nine, or 200 realizations, and for the different simulated signals with the highest SNR of 15 dB. Table I presents results of the RI where mean values and standard deviations over ten estimates are shown, for both algorithms, MSNSI and MTM, for the highest SNR of 15 dB. It is important to note that results for N_{rz} = 200 using the MSNSI algorithm (highlighted in red in Table I) are used as reference values to compare the performance of the algorithms in the different configurations tested. The results allow inferring that, from N_{rz} = 9, the variability of the RI measurements, represented by the standard deviation, is sufficiently reduced for both methods, where the relative errors between both methods are equal or less than 2%.

Based on these results, a number of nine realizations were established to compute the spectrogram, which presents a good tradeoff between variability and spatial resolution for in vivo applications, where the realizations are chosen as the eight-neighbor signals.

Table II presents the results of the RI for same signal of Fig. 3, where mean values and standard deviations over ten estimates are shown for both algorithms, MSNSI and MTM, as well as the peak frequency value. Results are shown for different simulated conditions varying the SNR from 1.5 to 15 dB and varying the sampling frequency from 800 to 2000 Hz.

Results were also obtained for two other signals (not shown), with peak frequencies of 570 and 480 Hz, signal 2 and signal 3, respectively.

For the cases with SNR values of 6 and 15 dB, when the sampling frequency is equal to or larger than twice the peak frequency (f_s = 2, 1.6 kHz for Signals 1 and 2, and f_s = 2, 1.6, and 1 kHz for Signal 3), both methods present similar results with relative errors less than 5% with respect to the reference values given in Table I. Moreover, when the sampling frequency is about or larger than 1.3 times and less than twice the peak frequency (f_s = 1 kHz for Signal 1, and f_s = 1 and 0.8 kHz for Signals 2 and 3), the MTM method presents relative errors below 7%, and the MSNSI method presents relative errors of up to 12%. When the sampling frequency is less than 1.5 the peak frequency (f_s = 0.8 kHz for Signal 1), relative errors ranged from 7% (SNR = 15 dB) to 13% (SNR = 6 dB) for the MTM method and from 22% to 33% for the MSNSI method.

For cases with SNR values of 1.5 and 4 dB, when the sampling frequency is equal to or larger than twice the peak frequency, the MTM method presents relative errors of less than 11%, and the MSNSI method presents relative errors of up to 48%. When the sampling frequency is about or larger than 1.5 times and less than twice the peak frequency, the MTM method presents relative errors below 7%, and the MSNSI method presents relative errors of up to 19%. When the sampling frequency is below the peak frequency of 1.5, relative errors were below 17% for the MTM method and 48% for the MSNSI method.

These results show that the MTM method performs better under limiting conditions than the MSNSI method for the type of signals studied. Thus, based on these results, some criteria were defined in order to guarantee relative errors below 10% in the measurement of RI. Therefore, only signals with an SNR higher than 5 dB were considered for computing the RI. From

TABLE II

RI COMPUTATION WHERE MEAN VALUES AND STANDARD DEVIATION OVER TEN ESTIMATES ARE SHOWN FOR SIGNAL$_1$ FOR VARIOUS SNRS AND SAMPLING FREQUENCIES. THE PEAK FREQUENCY, f_{pk}, CORRESPONDS TO 710 HZ

	MSNSI				MTM			
SNR (dB)	f_s = 2 kHz	f_s = 1.6 kHz	f_s = 1 kHz	f_s = 0.8 kHz	f_s = 2 kHz	f_s = 1.6 kHz	f_s = 1 kHz	f_s = 0.8 kHz
15	0.60 ± 0.01	0.59 ± 0.01	0.55 ± 0.01	0.47 ± 0.05	0.59 ± 0.01	0.59 ± 0.01	0.56 ± 0.01	0.56 ± 0.01
6.0	0.59 ± 0.01	0.57 ± 0.02	0.54 ± 0.02	0.38 ± 0.09	0.59 ± 0.01	0.59 ± 0.02	0.58 ± 0.01	0.52 ± 0.05
4.0	0.59 ± 0.02	0.55 ± 0.02	0.53 ± 0.02	0.31 ± 0.05	0.59 ± 0.01	0.59 ± 0.02	0.57 ± 0.02	0.50 ± 0.02
1.5	0.58 ± 0.02	0.56 ± 0.02	0.43 ± 0.05	0.33 ± 0.05	0.60 ± 0.02	0.59 ± 0.02	0.55 ± 0.02	0.55 ± 0.03

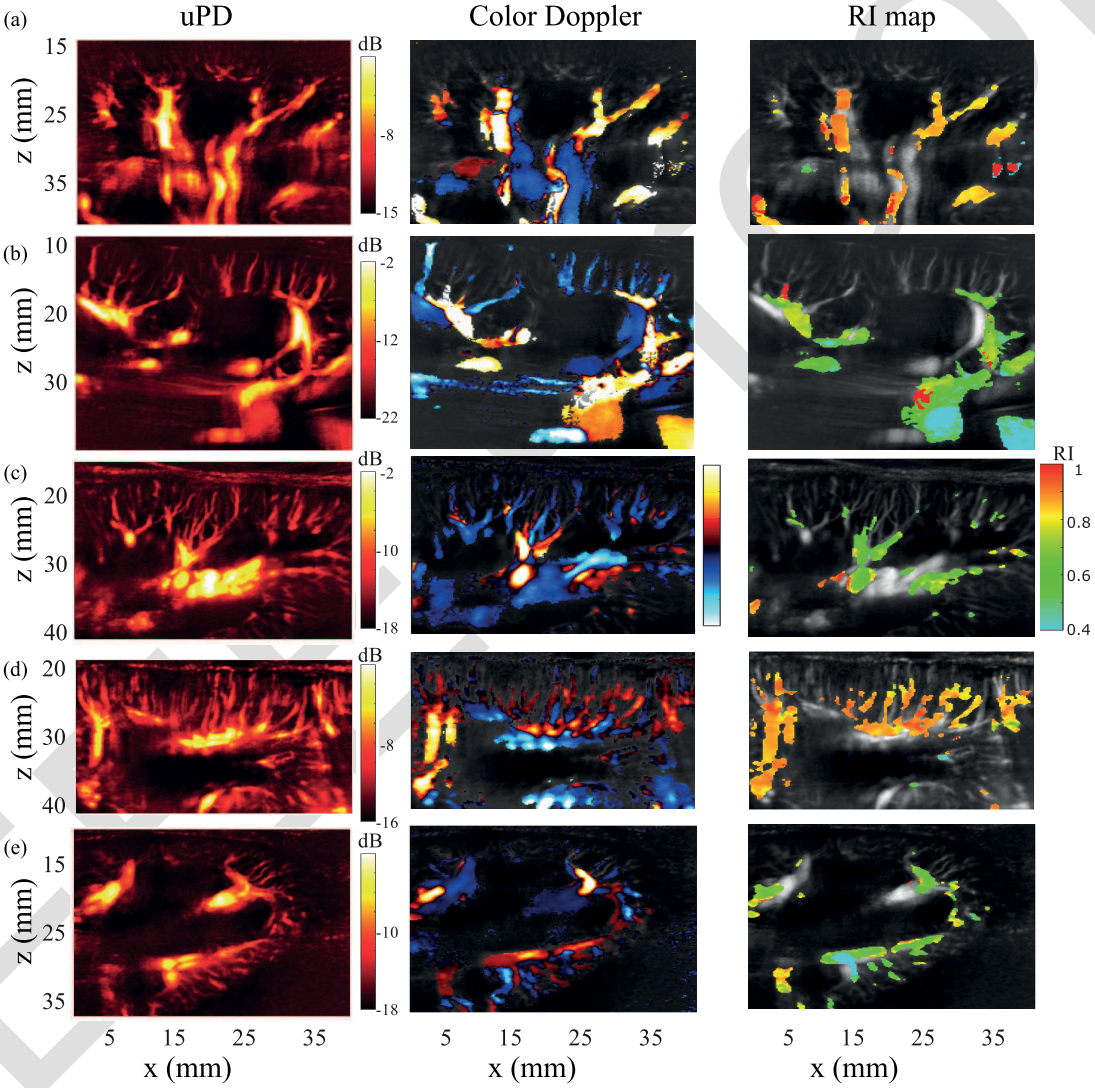

Fig. 5. Examples for five patient acquisitions of the uPD, color Doppler, and RI map for (a) patient 1, (b) patient 2, (c) patient 3, (d) patient 4, and (e) patient 5.

that, RI computation from signals with SNR between 5 and 10 dB was considered only if the peak frequency (related to the peak systolic velocity) was lower than 3/4 of the sampling frequency. If SNR was higher than 10 dB, the RI computation is considered even if the peak frequency is higher than 3/4 of the sampling frequency.

B. RI Measurements and Mapping

Fig. 5 shows the uPD, color Doppler images, and the RI map, obtained for the five patients from the uPWD acquisitions. It is recalled that regions in red, corresponding to RI values equal to 1, are not real RI measurements but an indication of pulsatile regions where the RI could not be measured correctly.

Fig. 6 shows a comparison between the PW Doppler method and the proposed method for measuring the RI on patient 2. For the PW Doppler measurement, the conventional color Doppler is shown, from which the radiologist manually detects a region of pulsatile flow, and in a subsequent step, the spectrogram is calculated, from which the radiologist determines the peak systolic and end-diastolic velocities to calculate the RI.

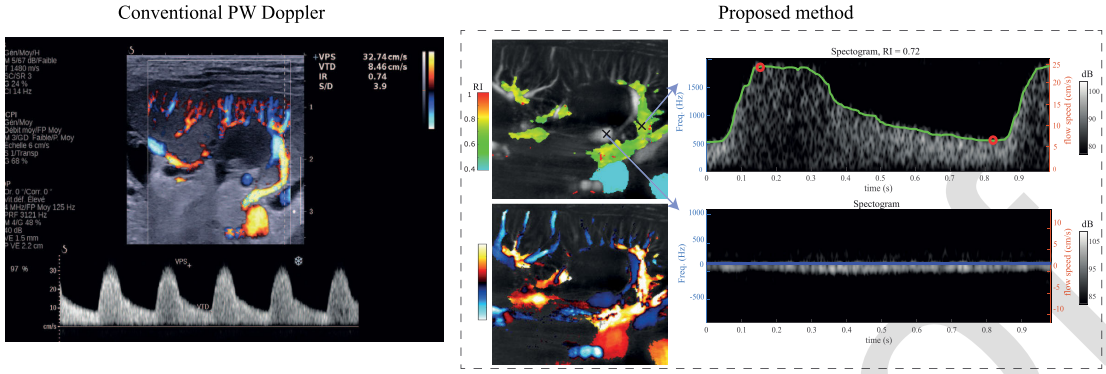

Fig. 6. Comparison between the RI measurements for patient 2 (acquisition 1) performed with PW Doppler and the proposed method on the same vessel. For the proposed method, the color Doppler image and RI map are displayed, as well as some examples of spectrograms. The red circles on the spectrograms represent the estimated end-systolic and end-diastolic velocities. For pulsatile flow, the velocities were 24.54 and 7.11 cm/s, respectively.

TABLE III

COMPARISON BETWEEN RI MEASUREMENTS FROM CLINICAL AND PROPOSED METHODS. RI FROM PW DOPPLER IS COMPUTED AS THE MEAN VALUE OF THE PERFORMED RI MEASUREMENTS, AND THE RI BASED ON THE PROPOSED METHOD CORRESPONDS TO THE MEDIAN OF THE RI MAP FOR EACH ACQUISITION. THE MEAN VALUE OF THE MEDIANS, $\overline{\text{RI}_{\text{acq}}}$, IS ALSO PRESENTED

Patient	$\overline{RI_{clinic}}$	Median of the RI map for each acquisiton								$\overline{RI_{acq}}$
		1	2	3	4	5	6	7	8	
1	0.86	0.86	0.81	0.87	0.83	0.86	0.83	0.86	0.85	0.85
2	0.73	0.67	0.71	0.64						0.67
3	0.60	0.66	0.67	0.70						0.68
4	0.91	0.89	0.83	0.86	0.91					0.87
5	0.63	0.72	0.69	0.67	0.61					0.68

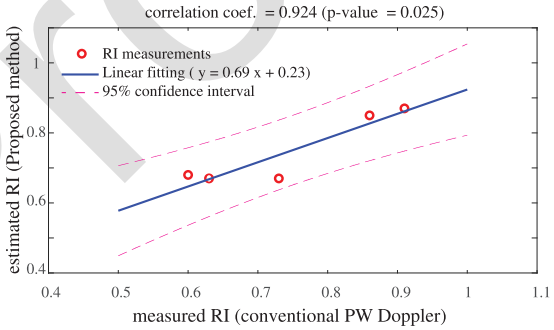

Fig. 7. Linear regression using the model $y = \beta x + b$ between results from PW Doppler and the proposed method, for which the mean value of the median values is used. For the proposed method, the mean value of medians is used. The correlation coefficient between measurements was of 0.924 (p-value = 0.025).

In the proposed approach, the RI map and the color Doppler image are shown, as well as examples of spectrograms for certain regions. The measurements obtained with the proposed method were compared with the measurements obtained with the conventional PW Doppler method for several patients, provided that it was possible to detect approximately the same region. A total of eight regions were detected, with relative errors of less than 11%.

On the other hand, it appears that the peak systolic and end-diastolic velocities are underestimated. However, a fair comparison cannot be made, as the way they are calculated by using PW Doppler is unknown, and they may differ slightly from the typical way, which is to use a scaling factor proportional to the speed of sound over the US frequency; the inclination of the flow with respect to the US beam could differ in both methods, as a result of variations in the acquisition plane. More details on the underestimation of these velocities by the MTM algorithm are presented in the discussion (see Section IV).

Table III shows, for each patient, the mean value of the RI measurements obtained by the PW Doppler method and the median of the RI map for each acquisition with its corresponding mean value. Note that RI values equal to 1 were not considered for the calculation of the median. When comparing results between the PW Doppler method and the proposed method for each acquisition, the relative errors ranged from 0% to 20%. When comparing the results obtained from PW Doppler with the mean value of the medians, the relative errors ranged from 1% to 15%.

Fig. 7 shows a linear regression between the results of PW Doppler and the proposed method, for which the mean value of the median values is used.

The correlation coefficient between the measurements is 0.924 (p-value = 0.025) and statistically significant considering a significance level of 5%. Although these results allow us to deduce that the measures present a good agreement since they present a significant coincidence, we must be careful with the conclusive observations derived from them since very few data were used.

IV. DISCUSSION

A. Limitations of Spectrogram Envelope Estimation

The baseline detection and MTM algorithms were developed and adapted by using typical signals from the renal uPWD acquisitions. From the simulated and in vivo results, the baseline detection algorithm performs well, and the MTM algorithm is computationally less expensive (about 40 times faster) and performs better under limited conditions than the MSNSI algorithm. At the time this article was prepared, we are not aware of any other algorithms reported in the literature with which the baseline detection algorithm can be compared.

However, their suitability for any other type of signals is something that needs to be studied further, for example, those of liver or umbilical, where RI measurements are also of interest in the clinic.

Another remark concerns the estimates of peak systolic and end-diastolic velocities. One can see from Fig. 4 that both algorithms tend to underestimate these velocities inasmuch the aliasing effects become important. The MSNSI algorithm presents a more important underestimation of the peak velocity than the end-diastolic velocity; on the other hand, the MTM underestimates both velocities to approximately the same extent. This may explain why the MTM performs better than the MSNSI in limited conditions when the aliasing effects are important, even if the peak systolic and end-diastolic velocities are underestimated.

This also put in evidence that the proposed method is not useful to estimate these velocities in most of the cases. Based on the simulation results, one could infer that the estimated velocities could be quite accurate when the peak velocity is lower than 3/4 of the velocity related to the sampling frequency and the SNR is higher than 10 dB.

Another limitation is that no spectral broadening effect has been considered in the proposed method, in the same way as for the calculation of the spectrogram from which the RI is measured by the conventional method, where, to the best of our knowledge, no correction is made. However, several works have shown the effects of spectral broadening on the estimation of the maximum velocity; most of the studies on this subject have been conducted under the assumption of using focused US beams but few in the case of unfocused US beams. The evaluation of the effects of spectral broadening on the estimation of the maximum velocity is not simple and requires extensive work since it depends on many parameters such as the flow velocity, the angle between the US beam and the flow direction, the characteristics of the US beam and the transducer, and the use of focused or unfocused US beams, among other factors [29], [30], [31], [32]. Thus, spectral broadening can play an important role in the estimation of RI in both the conventional and the proposed method, and its evaluation in the proposed method is something that will be studied in the future.

B. Limitations of the RI Computation Algorithm

In PW Doppler, once a region of pulsatile flow is detected, usually from color Doppler imaging, the radiologist has access to a spectrogram of the region of interest over several cardiac cycles. Once good repeatability of the spectrogram is observed across the cycles, the peak systolic velocity and end-diastolic velocity after peak systolic are manually estimated to calculate the RI. One of the advantages of this procedure is its robustness since the region for the RI calculation can be carefully chosen, and the frame rate can be increased above 2 kHz; however, one of the disadvantages is that it cannot be done everywhere and calculating the RI of 3 or more regions is time-consuming.

On the other hand, in the method proposed in this work, at most the spectrogram of a single cardiac cycle is obtained, with a maximal frame rate of 2 kHz. Consequently, the RI measurement proposed in this work is not as robust as in PW Doppler since the repeatability of the spectrogram over several cardiac cycles cannot be assessed. This repeatability is assumed in the proposed method. Moreover, only in some cases, RI measurement follows the procedure of estimating the end-diastolic velocity after the detected peak systolic. As for the 2-kHz frame rate and sequence duration of 1 s, these are the maximum values attainable for the programmed US sequence and are imposed by the US system.

For the reasons outlined above, the comparison between RI measurements performed by PW Doppler and the proposed point-to-point method could be biased. Therefore, the comparison was presented considering the median value of the RI map, as a way to look for a more robust indication of correlation between the two measurements.

Another possible limitation is related to the thresholds used in the proposed method in relation to SNR, the time elapsed between maximum and minimum velocities, and mean maximum frequency.

The SNR was selected based on simulated results by considering only pulsatile flow and random noise. However, it was observed that, in some cases, both pulsatile and nonpulsatile behaviors appeared in the spectrogram, but the one related to the pulsatile flow was strongly attenuated and sometimes showed aliasing so that it behaves as noise but differently than random noise, which is commonly assumed in simulations. Therefore, it would be interesting to perform further simulations by considering other noise sources and both kinds of flow, pulsatile and nonpulsatile.

The threshold used to check the maximum values of mean velocity was chosen based on the behavior of the experimental data. Although this definition gave good results in eliminating false pulsatile flows detected in most cases, more clinical data would be needed to better assess its suitability and define it more robustly. In addition, for this step, the mean frequency was calculated using the autocorrelation algorithm instead of the spectrogram-based method, as it presents better performance on signals with moderate aliasing, so signals with the highest velocity peaks (those represented with frequencies higher than $f_s - 100$ Hz) were excluded for the calculation of these thresholds.

On the other hand, an RI value of 0.4 was set as the minimum RI value, considering the clinician's recommendation, and the behavior of the nonpulsatile flow observed in the acquired signals. It was also considered that some pathologies are related to an increase in RI values, usually above 0.7 [33], [34], so that, in these conditions, it is not a real limitation. However, in cases where monitoring of RI values below 0.5 is required, definitely, the proposed method will be limited.

Finally, the results show that the plane wave imaging approach used is more sensitive than the conventional approach in terms of detecting small vessel flow. However, the corresponding acquired signals suffer from two limitations.

1) They have a low SNR, which makes quantitative analysis difficult.

2) The smaller they are, the closer they are, producing spectrograms with fluxes on both sides of the spectrum and a biased estimate of the mean axial velocity obtained by the autocorrelation method.

Therefore, the smaller vessels are only represented in the power Doppler image and are not considered in the quantitative analysis. This limitation may be imposed by the axial resolution, related to the width of the beam (about 0.2 mm), and remains a challenge in the proposed approach.

C. On RI Measurements and Mapping

Recent studies have shown that RI is related to inherent hemodynamic characteristics of patients [10], [11], so its current use, in which a punctual RI measurement is compared to a certain threshold, could be biased for diagnostic purposes. Thus, several studies have been conducted where RI has been combined with other biomarkers, for instance, with the central venous pressure, for the diagnosis of acute kidney injury (AKI) [35], as well as studies of the RI changes over time, for predicting mortality of renal transplant recipients [36]. These works showed that the combination of the RI with other biomarkers or other kinds of analysis of the RI could strive the potential misinterpretation of using only punctual RI measurements at a certain region. However, despite these limitations, the pilot study performed in this work presents promising results, as it provides a good estimate of the RI measurement, with relative errors of the order of 15%, which is currently of interest in the clinic. In addition, it provides a visualization of the RI behavior over the entire field of view that opens up new possibilities for the analysis and measurement of RI. For example, the RI map obtained as currently indicated could be used instead of color Doppler to detect regions of interest. In this way, the clinician will have access to the pulsatile flow directly and to preliminary RI measurements. This information will allow the clinician to more quickly detect regions of interest for RI calculation. Alternatively, the statistics of the RI map may also be studied for any correlation with renal states, which could provide new information not accessible so far. Another potential use is the combination with other biomarkers, such as stiffness provided by elastography [37], [38], or local pulse wave velocity [39], [40], which are accessible from ultrafast acquisitions.

The methodology proposed and studied in this work can be easily transferred and adapted to data acquired with curved probes. Therefore, in a further step, future studies will be carried out with the aim of transferring the proposed methodology to be used on data acquired with a curved probe with a center frequency of approximately 5 MHz, which is available on a more advanced US scanner available in the clinic, the Mach 30 from Hologic. This next step is important because curved probes offer a wider and deeper field of view with respect to linear probes, which is more advantageous for the clinician and is the main reason why they are preferred in the clinic for this type of application.

Finally, it is important to note that the calculation of the RI map assumes that the regions in which the RI is calculated correspond to arterial branches, in which the flow direction has a direction of preference toward the probe. This is the reason why only the RI has been calculated for such regions, and the RI has not been calculated for regions where the flow direction is away from the probe.

D. On Obtaining the RI Map in Real Time In Vivo

After data acquisition, the main steps to obtain the RI map consist of performing the clutter filtering using the SVD approach, followed by the calculation of the uPD image and its TGC compensation, and finally, the calculation and subsequent processing of the RI map over the entire field of view. The processing of a typical acquisition consisting of an IQ data array of $276 \times 192 \times 2000$ ($N_z \times N_x \times N_t$) takes approximately: 20 s for SVD filtering, 3 s for obtaining the uPD image compensated by TGC effects, and 900 s for obtaining the RI map. Recent works [41], [42] suggest that, in the near future, SVD filtering will be feasible in real time on the most advanced US platforms currently available in the clinic. As for the remaining stages, it is important to note that the developed algorithms can be further optimized, so there is a large margin for improvement in this aspect. At this stage, it is very difficult to estimate how far we could go in improving these codes in terms of computational time to be implemented in real time. However, this will be the subject of future studies in which the suitability and new opportunities offered by the proposed method for the clinical setting will be studied in greater depth. For this, a clinical study will be carried out in which a significant amount of data will be processed so that the developed algorithms will be optimized in order to reduce the computation time, and at this point, it will be possible to have a first evaluation of the feasibility of implementing this methodology in real time.

V. Conclusion

A method for calculating a 2-D color-coded RI map of the renal vasculature using clinical US equipment was developed and validated. The evaluation was carried out in the framework of a pilot study using Spectral Doppler measurements of the RI in renal transplanted patients. In addition, a tailored approach to kidney signals for spectrogram envelope detection, which is computationally less expensive and more perormant under limiting conditions than the one proposed by Kathpalia et al. [17], was proposed and evaluated by simulations. The main contributions of this work are given as follows.

1) To develop a methodology to obtain a 2-D color resistivity map of the renal vasculature that considers the effect of TGC and aliasing in the detection of pulsatile flow and the corresponding automatic calculation of RI.
2) The study conducted in this work demonstrated that the proposed method has the potential to provide the information currently required by clinicians and allows visualization of the pulsatile regions with the corresponding RI, which could be useful for clinicians from a diagnostic point of view.

APPENDIX
BASELINE DETECTION

The baseline detection is carried out as follows.

1) Once the flow direction is detected, the spectrogram is shifted K times to cover the range of frequencies f_k defined as

$$f_k = [-f_s/2 \pm 100k,\ f_s/2 \pm 100k]$$

where $\pm$ depends on the flow direction, and $k = 0, 1, 2, \ldots, K$, where $K = \lfloor f_s/200 \rfloor$, with $\lfloor \ldots \rfloor$ being the floor operator. This shifted spectrogram and frequencies, $\mathrm{SSTF}_k(x, z, f, t_0)$ and f_k, respectively, are used to compute the mean frequency $f_{\mathrm{m}_k}(x, z, t_0)$ and the relative error ε at each iteration k by

$$f_{\mathrm{m}_k}(x, z, t_0) = \frac{\int f_k \mathrm{SSTF}_k(x, z, f', t_0) df'}{\int \mathrm{SSTF}_k(x, z, f', t_0) df'}$$
$$\varepsilon_k = \sum_{t_0} |f_{\mathrm{m}_k}(x, z, t_0) - f_{\mathrm{m}_{k-1}}(x, z, t_0)| \quad (11)$$

respectively, where $f_{\mathrm{m}_k}(x, z, t_0)$ is smoothed by using a median filter of order 128.

2) Finally, the corrected spectrogram and frequencies are selected as the $\mathrm{SSTF}_{k_{\min}}(x, z, f, t_0)$, $f_{k_{\min}}$ such that $\varepsilon_{k_{\min}} = \min\{\varepsilon_k\}$.

REFERENCES

[1] J. Bercoff et al., "Ultrafast compound Doppler imaging: Providing full blood flow characterization," *IEEE Trans. Ultrason., Ferroelectr., Freq. Control*, vol. 58, no. 1, pp. 134–147, Jan. 2011.

[2] M. Tanter and M. Fink, "Ultrafast imaging in biomedical ultrasound," *IEEE Trans. Ultrason., Ferroelectr., Freq. Control*, vol. 61, no. 1, pp. 102–119, Jan. 2014.

[3] C. Demené et al., "Spatiotemporal clutter filtering of ultrafast ultrasound data highly increases Doppler and fUltrasound sensitivity," *IEEE Trans. Med. Imag.*, vol. 34, no. 11, pp. 2271–2285, Nov. 2015.

[4] K. Apelt, R. Bijkerk, F. Lebrin, and T. J. Rabelink, "Imaging the renal microcirculation in cell therapy," *Cells*, vol. 10, no. 5, p. 1087, May 2021.

[5] J. Provost et al., "Simultaneous positron emission tomography and ultrafast ultrasound for hybrid molecular, anatomical and functional imaging," *Nature Biomed. Eng.*, vol. 2, no. 2, pp. 85–94, Feb. 2018.

[6] M. Perez-Liva et al., "Performance evaluation of the PET component of a hybrid PET/CT-ultrafast ultrasound imaging instrument," *Phys. Med. Biol.*, vol. 63, no. 19, Sep. 2018, Art. no. 19NT01.

[7] J. Radermacher, S. Ellis, and H. Haller, "Renal resistance index and progression of renal disease," *Hypertension*, vol. 39, no. 2, pp. 699–703, Feb. 2002.

[8] R. Ikee et al., "Correlation between the resistive index by Doppler ultrasound and kidney function and histology," *Amer. J. Kidney Diseases*, vol. 46, no. 4, pp. 603–609, Oct. 2005.

[9] T. Sugiura and A. Wada, "Resistive index predicts renal prognosis in chronic kidney disease," *Nephrology Dialysis Transplantation*, vol. 24, no. 9, pp. 2780–2785, Sep. 2009.

[10] M. Naesens et al., "Intrarenal resistive index after renal transplantation," *New England J. Med.*, vol. 369, no. 19, pp. 1797–1806, Nov. 2013, doi: 10.1056/NEJMoa1301064.

[11] P. Di Nicolo and A. Granata, "Renal intraparenchymal resistive index: The ultrasonographic answer to many clinical questions," *J. Nephrology*, vol. 32, no. 4, pp. 527–538, Aug. 2019.

[12] C. Demené, J. Mairesse, J. Baranger, M. Tanter, and O. Baud, "Ultrafast Doppler for neonatal brain imaging," *NeuroImage*, vol. 185, pp. 851–856, Jan. 2019. [Online]. Available: https://www.sciencedirect.com/science/article/pii/S1053811918303008

[13] S. Franchi-Abella, "Applications de l'imagerie ultrasonore ultrarapide aux pathologies hépatiques diffuses de l'enfant," Ph.D. dissertation, Dept. Phys., Sorbonne Paris Cite, Paris, France, 2015.

[14] P. Song, A. Manduca, J. D. Trzasko, and S. Chen, "Ultrasound small vessel imaging with block-wise adaptive local clutter filtering," *IEEE Trans. Med. Imag.*, vol. 36, no. 1, pp. 251–262, Jan. 2017.

[15] P. Song, A. Manduca, J. D. Trzasko, and S. Chen, "Noise equalization for ultrafast plane wave microvessel imaging," *IEEE Trans. Ultrason., Ferroelectr., Freq. Control*, vol. 64, no. 11, pp. 1776–1781, Nov. 2017.

[16] G. Cloutier, F. Lemire, L.-G. Durand, Y. Latour, and Y. E. Langlois, "Computer evaluation of Doppler spectral envelope area in patients having a valvular aortic stenosis," *Ultrasound Med. Biol.*, vol. 16, no. 3, pp. 247–260, Jan. 1990.

[17] A. Kathpalia et al., "Adaptive spectral envelope estimation for Doppler ultrasound," *IEEE Trans. Ultrason., Ferroelectr., Freq. Control*, vol. 63, no. 11, pp. 1825–1838, Nov. 2016.

[18] J. Latham, Y. Hicks, X. Yang, R. Setchi, and T. Rainer, "Stable automatic envelope estimation for noisy Doppler ultrasound," *IEEE Trans. Ultrason., Ferroelectr., Freq. Control*, vol. 68, no. 3, pp. 465–481, Mar. 2021.

[19] R. Nayak, M. Fatemi, and A. Alizad, "Adaptive background noise bias suppression in contrast-free ultrasound microvascular imaging," *Phys. Med. Biol.*, vol. 64, no. 24, Dec. 2019, Art. no. 245015, doi: 10.1088/1361-6560/ab5879.

[20] M. Bayat, M. Fatemi, and A. Alizad, "Background removal and vessel filtering of noncontrast ultrasound images of microvasculature," *IEEE Trans. Biomed. Eng.*, vol. 66, no. 3, pp. 831–842, Mar. 2019.

[21] S. Adabi, S. Ghavami, M. Fatemi, and A. Alizad, "Non-local based denoising framework for in vivo contrast-free ultrasound microvessel imaging," *Sensors*, vol. 19, no. 2, p. 245, Jan. 2019.

[22] C. Huang, P. Song, P. Gong, J. D. Trzasko, A. Manduca, and S. Chen, "Debiasing-based noise suppression for ultrafast ultrasound microvessel imaging," *IEEE Trans. Ultrason., Ferroelectr., Freq. Control*, vol. 66, no. 8, pp. 1281–1291, Aug. 2019.

[23] R. C. Gessner, S. R. Aylward, and P. A. Dayton, "Mapping microvasculature with acoustic angiography yields quantifiable differences between healthy and tumor-bearing tissue volumes in a rodent model," *Radiology*, vol. 264, no. 3, pp. 733–740, Sep. 2012, doi: 10.1148/radiol.12112000.

[24] S. E. Shelton et al., "Quantification of microvascular tortuosity during tumor evolution using acoustic angiography," *Ultrasound Med. Biol.*, vol. 41, no. 7, pp. 1896–1904, Jul. 2015. [Online]. Available: https://www.sciencedirect.com/science/article/pii/S0301562915002069

[25] L. Chinchilla, T. Frappart, C. Fraschini, J.-M. Correas, and J.-L. Gennisson, "Adaptive compensation of TGC effects in contrast-free ultrasensitive ultrasound Doppler imaging for improved resistivity index map visualization," in *Proc. IEEE Int. Ultrason. Symp. (IUS)*, Sep. 2021, pp. 1–4.

[26] L. Y. L. Mo and R. S. C. Cobbold, "'Speckle' in continuous wave Doppler ultrasound spectra: A simulation study," *IEEE Trans. Ultrason., Ferroelectr., Freq. Control*, vol. UFFC-33, no. 6, pp. 747–753, Nov. 1986.

[27] J. Baranger, B. Arnal, F. Perren, O. Baud, M. Tanter, and C. Demené, "Adaptive spatiotemporal SVD clutter filtering for ultrafast Doppler imaging using similarity of spatial singular vectors," *IEEE Trans. Med. Imag.*, vol. 37, no. 7, pp. 1574–1586, Jul. 2018.

[28] K. Marasek and A. Nowicki, "Comparison of the performance of three maximum Doppler frequency estimators coupled with different spectral estimation methods," *Ultrasound Med. Biol.*, vol. 20, no. 7, pp. 629–638, 1994.

[29] G. Cloutier, K. K. Shung, and L.-G. Durand, "Experimental evaluation of intrinsic and nonstationary ultrasonic Doppler spectral broadening in steady and pulsatile flow loop models," *IEEE Trans. Ultrason., Ferroelectr., Freq. Control*, vol. 40, no. 6, pp. 786–795, Nov. 1993.

[30] A. J. Winkler and J. Wu, "Correction of intrinsic spectral broadening errors in Doppler peak velocity measurements made with phased sector and linear array transducers," *Ultrasound Med. Biol.*, vol. 21, no. 8, pp. 1029–1035, Jan. 1995.

[31] G. Guidi, C. Licciardello, and S. Falteri, "Intrinsic spectral broadening (ISB) in ultrasound Doppler as a combination of transit time and local geometrical broadening," *Ultrasound Med. Biol.*, vol. 26, no. 5, pp. 853–862, Jun. 2000. [Online]. Available: https://www.sciencedirect.com/science/article/pii/S0301562900002180

[32] B.-F. Osmanski, J. Bercoff, G. Montaldo, T. Loupas, M. Fink, and M. Tanter, "Cancellation of Doppler intrinsic spectral broadening using ultrafast Doppler imaging," *IEEE Trans. Ultrason., Ferroelectr., Freq. Control*, vol. 61, no. 8, pp. 1396–1408, Aug. 2014.

[33] S. Samoni et al., "The relationship between intra-parenchymal renal resistive index variation and renal functional reserve in healthy subjects," *J. Nephrology*, vol. 34, no. 2, pp. 403–409, Apr. 2021.
[34] D. B. Rukstalis and P. F. Fulgham, *Renal Ultrasound*. Cham, Switzerland: Springer, 2021, pp. 51–72, doi: 10.1007/978-3-030-52309-1_5.
[35] J. Song, W. Wu, Y. He, S. Lin, D. Zhu, and M. Zhong, "Value of the combination of renal resistance index and central venous pressure in the early prediction of sepsis-induced acute kidney injury," *J. Crit. Care*, vol. 45, pp. 204–208, Jun. 2018. [Online]. Available: https://www.sciencedirect.com/science/article/pii/S0883944117315344
[36] J.-B. de Freminville et al., "Early changes in renal resistive index and mortality in diabetic and nondiabetic kidney transplant recipients: A cohort study," *BMC Nephrology*, vol. 22, no. 1, pp. 1–12, Dec. 2021.
[37] J.-L. Gennisson, N. Grenier, C. Combe, and M. Tanter, "Supersonic shear wave elastography of in vivo pig kidney: Influence of blood pressure, urinary pressure and tissue anisotropy," *Ultrasound Med. Biol.*, vol. 38, no. 9, pp. 1559–1567, Sep. 2012.
[38] N. Grenier, J.-L. Gennisson, F. Cornelis, Y. L. Bras, and L. Couzi, "Renal ultrasound elastography," *Diagnostic Interventional Imag.*, vol. 94, no. 5, pp. 545–550, 2013, [Online]. Available: https://www.sciencedirect.com/science/article/pii/S2211568413000387
[39] M. Couade et al., "Ultrafast imaging of the arterial pulse wave," *IRBM*, vol. 32, no. 2, pp. 106–108, Apr. 2011.
[40] L. X. Yin et al., "Reference values of carotid ultrafast pulse-wave velocity: A prospective, multicenter, population-based study," *J. Amer. Soc. Echocardiogr.*, vol. 34, no. 6, pp. 629–641, 2021.
[41] P. Song et al., "Accelerated singular value-based ultrasound blood flow clutter filtering with randomized singular value decomposition and randomized spatial downsampling," *IEEE Trans. Ultrason., Ferroelectr., Freq. Control*, vol. 64, no. 4, pp. 706–716, Apr. 2017.
[42] U.-W. Lok et al., "Real time SVD-based clutter filtering using randomized singular value decomposition and spatial downsampling for micro-vessel imaging on a verasonics ultrasound system," *Ultrasonics*, vol. 107, Sep. 2020, Art. no. 106163.

Lenin Chinchilla was born in Bucaramanga, Colombia, in 1986. He received the Electronic Engineering and Physicist degrees and the master's degree in electronic engineering from the Universidad Industrial de Santander, Bucaramanga, in 2011, 2012, and 2015, respectively, and the Ph.D. degree in engineering sciences, specialty acoustics, from AIX-Marseille University, Marseille, France, in cotutelle with Roma TRE University, Rome, Italy, in 2020.

Since 2020, he has been a Postdoctoral Researcher with the Multimodal Biomedical Imaging Research Laboratory, Biomaps, Université Paris-Saclay, Orsay, France, working mainly on the development of new imaging modalities based on the ultrafast ultrasound imaging approach. His current research interests include quantitative ultrasound techniques, ultrasound tissue characterization, ultrafast ultrasound imaging, and signal processing.

Thomas Flappart received the Diplôme d'ingénieur degree in physics from the Ecole Supérieure de Physique et de Chimie Industrielles de Paris (ESPCI), Paris, France, in 2010, and the M.S. degree in acoustics from Paris VII University, Paris, in 2012.

After the master's degree, he joined SuperSonic Imagine. His research interests include the medical applications of ultrasound, mainly shear wave elastography, and blood flow analysis.

Christophe Fraschini, photograph and biography not available at the time of publication.

Jean-Michel Correas received the Ph.D. degree from the University of Tours.

He is a Professor of Radiology at the Paris-Descartes University and Vice-Chairperson at the Department of Adult Radiology in Necker University Hospital, Paris, France since 2006. He was a Visiting Professor of Radiology at the University of Toronto department of Imaging Research, where he was in charge of several research projects on Ultrasound Contrast Agents as part of his doctorate of science on Ultrasound Contrast Agents. He is also involved in diagnostic and interventional imaging of liver and renal cancer. Since 2010, he is involved with the development and evaluation of a novel imaging technique that allows non-invasive assessment of tissue stiffness, ultrasound elastography. His main research interests include ultrasound elastography, contrast-enhanced ultrasound, ultrafast ultrasound imaging, renal transplant imaging including ultrasound and Magnetic Resonance Imaging (MRI), percutaneous ablation of tumors, combined ultrasound and multimodality fusion.

Jean-Luc Gennisson (Member, IEEE) received the Ph.D. degree in physics from Paris VI University, Paris, France, in 2003.

He is currently a Research Professor (Directeur de Recherche) with the French National Research Center (CNRS), Paris. For four years, he has been heading the team "Methodological Development and Instrumentation" at the BioMaps Laboratory, Commissariat à l'Energie Atomique et aux Energies Alternatives (CEA), Service Hospitalier Frédéric Joliot (SHFJ), Orsay, France. His main activities are centered on the development of new approaches in wave physics for medical imaging and therapy. He is a recipient of 16 patents in the field of ultrasound imaging. He is the author of more than 130 technical peer-reviewed papers and book chapters. His current research interests include multiple topics: shear wave elastography, ultrafast ultrasound imaging, ultrasensitive Doppler imaging, functional ultrasound imaging, ultrasound therapy, low and high field Magnetic Resonance Imaging (MRI) and Magnetic Resonance Elastography (MRE), positron emission tomography (PET) imaging, and multimodality imaging.

Dr. Gennisson received the Outstanding Paper Award from IEEE Ultrasonics, Ferroelectrics, and Frequency Control (UFFC) in 2015 for his work on "4-D ultrafast shear wave imaging."